Spatial distributions of ions and electrons from the plasma sheet to the inner magnetosphere: Comparisons between THEMIS-Geotail statistical results and the Rice convection model

Chih-Ping Wang,[1] Matina Gkioulidou,[1] Larry R. Lyons,[1] Richard A. Wolf,[2] Vassilis Angelopoulos,[3] Tsugunobu Nagai,[4] James M. Weygand,[5] and A. T. Y. Lui[6]

[1] To understand the processes responsible for the formation and structure of plasma sheet and ring current particles, we have used THEMIS and Geotail data to investigate statistically the distributions of ions and electrons from the midtail to the inner magnetosphere and compared them with results from the Rice convection model (RCM). The observed distributions show clear magnetic local time (MLT) asymmetries in the thermal energy and energy fluxes of plasma sheet particles but many more MLT symmetric ring current particles. Our RCM runs include both self-consistent electric and magnetic fields and realistic MLT-dependent outer particle sources. Starting with no initial particles, particles released from the RCM outer sources move along electric and magnetic drift paths and change energy adiabatically. Comparison of the observation with the simulation indicates that the particles along the open drift paths can account for the observed plasma sheet populations and that the observed significant MLT variations are a combined result of species- and energy-dependent drift and location-dependent source strength. The simulated energy and spatial distributions of the particles within closed drift paths are found to be consistent with the observed ring current particles. These ring current particles are originally plasma sheet particles which became trapped along closed paths due to temporal variations of drift paths. The good agreement in key features of the spatial distributions of thermal energy and energy fluxes between the RCM and observations clearly indicates that electric and magnetic drift transport and the associated energization play dominant roles in plasma sheet and ring current dynamics.

1. Introduction

[2] Dynamic changes in the spatial structure of plasma sheet and ring current ions and electrons in the near-Earth magnetosphere in response to solar wind and interplanetary magnetic field (IMF) variations result in geomagnetic storms and substorms. Kinetic simulations have suggested key processes responsible for the formation and spatial structure of these particle distributions: (1) particles are transported mainly by adiabatic electric and magnetic drift and change energy adiabatically, (2) the drift paths are significantly affected by the imposed solar wind convection, as well as by the electromagnetic coupling between the plasma sheet and the ionosphere, and (3) the main source for ring current particles is tail plasma sheet particles that originally come from either the solar wind or ionosphere. A global spatial structure extending continuously from the tail plasma sheet into the ring current is thus necessary for investigating the above key processes. However, due to the limited region covered by spacecraft, previous investigations of the spatial structures have only focused on either the inner magnetosphere or the plasma sheet (for example, the inner magnetosphere from AMPTE [e.g., *Milillo et al.*, 2001], CRRES [*Korth et al.*,

[1]Department of Atmospheric and Oceanic Sciences, University of California, Los Angeles, California, USA.

[2]Department of Physics and Astronomy, Rice University, Houston, Texas, USA.

[3]Department of Earth and Space Sciences, University of California, Los Angeles, California, USA.

[4]Department of Earth and Planetary Sciences, Tokyo Institute of Technology, Tokyo, Japan.

[5]Institute of Geophysics and Planetary Physics, University of California, Los Angeles, California, USA.

[6]Johns Hopkins University Applied Physics Laboratory, Laurel, Maryland, USA.

2000], and Polar [*Roeder et al.*, 2005] and the plasma sheet from Geotail [e.g., *Wang et al.*, 2006]). Therefore, in this study we combined data set from different spacecraft to establish the global structures by using the THEMIS observations in the inner magnetosphere and the Geotail measurement in the plasma sheet.

[3] We previously analyzed the Geotail data statistically within the nightside plasma sheet region $30 R_E > r > 8 R_E$ to determine the plasma sheet structure under different interplanetary conditions and AE levels [*Wang et al.*, 2006, 2007, 2009]. Our evaluation of Geotail spatial distributions shows that adiabatic electric and magnetic drift is important for transporting particles near and above the thermal energy within the tail plasma sheet. However, since Geotail data is not available earthward of $r = 8 R_E$ we could not verify if these plasma sheet particles continue their electric and magnetic drift into the inner magnetosphere. On the other hand, we have previously investigated the radial profiles of particle distributions from $r \sim 4$–$12 R_E$ using observations from THEMIS spacecraft that passed through almost the same duskside magnetic local time (MLT) during different phases of a weak storm [*Wang et al.*, 2008] near the beginning of the THEMIS mission. The observed radial profiles indicate that earthward penetration of the plasma sheet under storm-time enhanced convection results in an increase of ring current particles, and that changes of the earthward edge of the plasma sheet with convection strength are consistent with theoretical predictions of the inner edges of open drift paths connected to the tail plasma sheet region. Since then, THEMIS have passed the inner magnetosphere at all MLTs many times, which has provided further verification of the above conclusions for the electron inner edges at different MLT [*Kurita et al.*, 2011; *Jiang et al.*, 2011].

[4] There are a variety of kinetic ring current simulations with different specifications of adiabatic conservation parameters, particle sources, electric and magnetic fields, and coupling with the ionosphere [e.g., *Chen et al.*, 2006; *Fok et al.*, 2010; *Jordanova et al.*, 2010]. Most of the ring current simulations are confined only to the inner magnetosphere. There have been some comparisons with in situ THEMIS data or the particle distributions inferred from IMAGE data [e.g., *Fok et al.*, 2010; *Buzulukova et al.*, 2010], but the observations are also limited to the inner magnetosphere. The Rice convection model (RCM) computes electric and magnetic drift of isotropic ions and electrons with electric field changing self-consistently through conservation of current continuity in both the magnetosphere and ionosphere [*Toffoletto et al.*, 2003]. Previously, we have extended the RCM outer boundary to $X = -20 R_E$ so that transport of the plasma sheet particles from the midtail can be included, and we have incorporated the RCM with more realistic particle boundary conditions from the Geotail data that depend on MLT as well as on the solar wind and IMF conditions [*Gkioulidou et al.*, 2009]. As described in the companion paper [*Gkioulidou et al.*, 2011, hereinafter Paper 1], we have also incorporated the RCM with a magnetic field solver that provides fields that are in force balance with the RCM plasma pressure in the equatorial plane. With this force balanced field, we are able to more accurately model particle drift and the resulting spatial distributions than with our previous RCM simulations under non-force-balanced Tsyganenko 96 magnetic fields.

[5] By combining THEMIS and Geotail observations in this study, we first established the average spatial distributions of ions and electrons from the midtail to inner magnetosphere under two different convection strengths. We then conducted the RCM runs with self-consistent electric and magnetic fields and with realistic boundary particle conditions that match the observations at the model boundary locations. We started the runs with no particles so that particles must originally come from the outer boundary. The simulation results are found to well reproduce key features seen in the observed spatial structure of plasma sheet and ring current particles, thus clearly indicating the crucial roles of the above key processes used in kinetic models in the formation of the plasma sheet and ring current. We identify and discuss the physical processes that account for the observed key features. We also discuss the differences between the simulations and observations, which are likely due to processes that are associated with temporal fluctuations in convection strength and particle sources that were not realistically specified in our current simulation runs.

2. Observational Results

2.1. Data Selections

[6] In this study we used THEMIS observation from 23 March 2007 to 30 April 2010 and Geotail data from 1 January 1995 to 31 December 2005. Geotail data from 1996 was not used since the AE index for 1996 was not available before completion of this study. Geotail data from after 2006 was also not used because Geotail stayed mostly at higher latitudes in the magnetotail after 2006. Aberrated GSM coordinates (with the aberration angle determined by 1 hour averaged solar wind velocity) are used. Geotail covers regions from $r \sim 8$–$30 R_E$. In our selected THEMIS periods, three of the five THEMIS spacecraft cover regions inside $r \sim 12 R_E$, while the other two cover regions inside $r \sim 30 R_E$. Therefore, by combining these two data sets we obtain observations of the magnetosphere from $r \sim 30 R_E$ on the nightside to the dayside magnetopause. (Note that there is no time overlap for the selected Geotail and THEMIS data. The overall THEMIS fluxes in the overlap region are found to be smaller than the Geotail fluxes (up to a factor of 2), likely due to the corresponding solar wind density in the selected THEMIS period (average ~ 4 cm^{-3}) being lower than that in the selected Geotail period (average ~ 6.5 cm^{-3}).) Plasma data from two instruments on board Geotail are used: the ion and electron data from the Low Energy Particle (LEP) instrument [*Mukai et al.*, 1994] that covers the ion energy range from 21 eV/q to 44 keV/q and the electron energy range from 43 eV to 41 keV, and the proton data from the Energetic Particles and Ion Composition (EPIC) instrument [*Williams et al.*, 1994] that covers the energy range from 46 keV to 3005 keV. Magnetic field data is from the magnetic field (MGF) experiment [*Kokubun et al.*, 1994]. The ion moments are from a summation of the LEP and EPIC data and the electron moments are only from the LEP data. One minute averages of the Geotail plasma and magnetic field data are used.

[7] For THEMIS, the ions and electrons are measured by an electrostatic analyzer (ESA, 0.006–20 keV/q for ions and 0.007–26 keV for electrons [*McFadden et al.*, 2008a]) and a solid state telescope (SST, 35 keV–6 MeV for ions and 30 keV–6 MeV for electrons). Full distributions are used with time resolution of a few minutes. For each measured energy spectrum, contamination to ESA and SST is removed. The penetrating radiation contamination is removed from the ESA data by subtracting the minimum count value within the ESA energy ranges (see Appendix A). The sunlight contamination to the SST is removed (defined by a criteria that considers a data point being contaminated if its modified z score calculated across azimuthal angle is greater than 3.5. The modified z score is a normalized outlier detection test [*Iglewicz and Hoaglin*, 1993]. For a data point with value x_i, its modified z score is $0.6745 \cdot (x_i - x_{\mathrm{median}})/\mathrm{median}(|x_i - x_{\mathrm{median}}|))$. For ions, there is energy gap (from ~20 to 28 keV) between the highest ESA channel and the lowest SST channel. We interpolate the fluxes for this energy gap using the fluxes from the two nearby energy channels. The total plasma moments are a summation of the ESA and SST moments. For both Geotail and THEMIS, omnidirectional particle fluxes are used. The magnetic field is measured by the FGM instrument [*Auster et al.*, 2008].

[8] The plasma sheet is centered at the equatorial plane. Central plasma sheet crossings are selected when plasma β (defined as $(P_{\mathrm{ion}} + P_{\mathrm{electron}})/(B^2/(2\mu_0))$) satisfies the criteria: $\beta \geq 1$, for $r \geq 15\ R_E$ and $\beta \geq 10^{0.14r - 2.1}$ for $r < 15\ R_E$. The β criteria is r dependent since β in the equatorial plane decreases with decreasing r. We use $V_x > -100$ km/s and ion temperature >0.5 keV near typical magnetopause locations to exclude magnetosheath crossings. From total plasma pressure ($P_{\mathrm{ion}} + P_{\mathrm{electron}}$) and magnetic field measurements, we estimate the flux tube volume V using a formula based on a simple two-dimensional analytic model of plasma in force equilibrium [*Wolf et al.*, 2006]. The estimated V is used only when the perpendicular flow is slow ($V_\perp \leq 100$ km/s) and

$$\sqrt{\left(B_x^2 + B_y^2\right)}/B_z \leq 3,$$

a condition under which Wolf et al. found that their formula provides good estimates. The flux tube volume formula was found to perform very well (RMS err/mean ~0.16) in tests involving force equilibrium magnetic field configurations.

[9] The objective of this study is to compare the observed large-scale particle spatial structure with the RCM simulations. Since the external driver for the RCM is the cross polar cap potential drop ($\Delta\Phi_{\mathrm{PC}}$), to make the comparisons more appropriate we separated the observational data according to their corresponding $\Delta\Phi_{\mathrm{PC}}$. $\Delta\Phi_{\mathrm{PC}}$ is estimated using the Weimer empirical model [*Weimer*, 1995], which depends on the IMF B_y, IMF B_z, and the solar wind speed. We used the solar wind and IMF data mainly from Wind. The arrival time of the IMF at the subsolar bow shock at ($X = 17$, $Y = 0$, $Z = 0\ R_E$) is determined by calculating the minimum variance direction using the minimum variance analysis technique [*Weimer et al.*, 2003; *Weimer*, 2004]. During times when the Wind data is not available or the propagated Wind data is not reliable due to the Wind's position (when Wind is more than ~50 R_E off the Sun-Earth), we used the solar wind and IMF data from ACE, which is available after February 1998.

[10] Limited by the number of data points available for determining a spatial structure globally, we simply divided the data to correspond to either low and high convection strength. However, even under the same convection strength, there are periods of the substorm expansion and recovery phases during which frequent and relatively large mesoscale changes occur in the magnetosphere. These mesoscale changes are likely caused by local processes, but it is not yet clear on how these processes may be directly related to solar wind driving. While the solar wind energy input into magnetosphere and the resulting changes within the magnetosphere are relatively steady during the substorm growth phases. For the goal of this study to compare with the RCM simulations with simple driving conditions, we want the observation to better represent particle distributions resulting from large-scale and relatively steady transport. Therefore, we minimize the periods of the substorm expansion and recovery phases in the data set by restricting the data point to also correspond to lower AE levels since the occurrence rate of the substorm expansion and recovery phases is higher when AE is higher. Thus individual Geotail and THEMIS observations in the central plasma sheet are sorted into 2 different convection levels according to the $\Delta\Phi_{\mathrm{PC}}$ and AE index averaged over the 1 h period prior to that observation: (1) weak convection: $20 < \Delta\Phi_{\mathrm{PC}} < 40$ kV, $10 < \mathrm{AE} < 50$ nT and (2) strong convection: $50 < \Delta\Phi_{\mathrm{PC}} < 100$ kV, $50 < \mathrm{AE} < 150$ nT. Note that there are no $\Delta\Phi_{\mathrm{PC}}$ smaller than 22 kV from the Weimer empirical model [*Weimer*, 1995] and the occurrence rate becomes quite small for $\Delta\Phi_{\mathrm{PC}}$ larger than 100 kV. The AE level is elevated during the substorm growth phase compared to that during quiet times so that a higher AE range is used for the strong convection level. The $\Delta\Phi_{\mathrm{PC}}$ and AE ranges used in our criteria are chosen to maximize the number of data points for each of the two levels for this statistical study. Stricter criteria (narrower $\Delta\Phi_{\mathrm{PC}}$ ranges) gave global distributions with key features similar to those using the current criteria, but spatial coverage in the distributions became less complete. (Also note that there have been RCM runs attempting to investigate quantitatively particle transport associated with the substorm expansion phase [e.g., *Zhang et al.*, 2009; *Yang et al.*, 2011], but coordinating comparisons of their simulations with our observations for high AE level is beyond the scope of this study.) The number of selected data within each 1 $R_E \times 1\ R_E$ areas in the X-Y plane for the two convection levels are shown in Figure 1. There are more data selected corresponding to weak convection, likely due to the plasma sheet being relatively thicker under weak convection.

2.2. Observed Energy Spectrums of Plasma Sheet and Ring Current Ions and Electrons at Different MLT

[11] Figures 2 and 3 show the median values of ion and electron energy fluxes, respectively, versus energy along 8 different MLT meridians for the two convection levels. To indicate statistically how much energy flux varies within each energy channel at a fixed location under each of the two convection levels, we plot in the bottom of Figures 2 and 3 the percentiles of energy fluxes versus energy at midnight midtail at $X = -20\ R_E$ and at dawn and dusk at $r = 5\ R_E$. These percentiles are illustrated as the minimum (25%) and maximum (75%) of the error bar, and the line
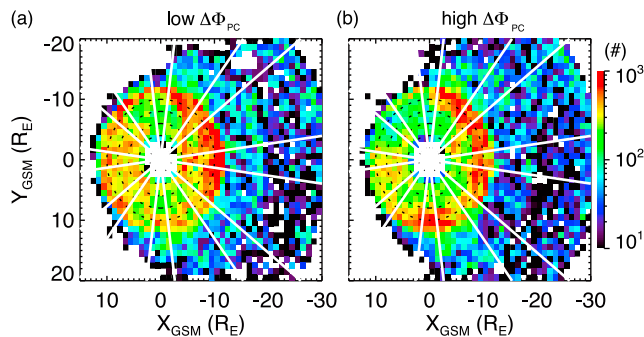
Figure 1. Number of measurements during periods of the (a) low convection level and (b) high convection level. The white straight lines indicate the magnetic local time (MLT) meridians along which the energy spectrums are shown in Figure 2.

corresponds to the median. Two main populations can be clearly identified from the peaks of energy fluxes: (1) plasma sheet populations outside radial distance $r > \sim 4\ R_E$ and (2) a relatively higher energy ring current population inside $r \sim 10\ R_E$. The two populations coexist in the region $r \sim 4$–$10\ R_E$. For plasma sheet populations, the ion thermal energy (as indicated by the peaks in energy fluxes) during weak convection is about 5 keV at $r = 30\ R_E$ at midnight and increases with decreasing r. The increase is more pronounced at the premidnight than the postmidnight MLTs, resulting in higher ion thermal energy at dusk ($\gtrsim 10$ keV) than at dawn ($\lesssim 10$ keV) in the near-Earth region. As a result, the population shows a clear dawn-dusk asymmetry with fluxes of cooler plasma sheet ions ($\lesssim 5$ keV) being substantially higher at dawn than at dusk, as can be seen from the percentiles shown in Figure 2c. For the plasma sheet electrons, the thermal energy increases from $\lesssim 1$ keV at the tail to a few keV at the near-Earth region, with higher energy in the postmidnight ($\lesssim 10$ keV at dawn) than the premidnight sector ($\lesssim 2$ keV at dusk), opposite to the asymmetry seen in ions. For ring current particles, the ion thermal energy increases sharply with decreasing r from 10 s of keV at $r \sim 10\ R_E$ to a few hundreds of keV inside $r \sim 6\ R_E$. For ring current electrons, energy fluxes only show distinguishable peaks inside $r \sim 6\ R_E$ with the thermal energy being $\gtrsim 100$ keV and not strongly depend on r. Unlike the strong MLT asymmetries seen in the plasma sheet populations, the thermal energy of ring current particles is rather symmetric in MLT, as can be also seen in Figures 2c and 3c. Figure 2c also shows that in the inner magnetosphere, the thermal energy peak of plasma sheet ions is more distinctly separated from that of ring current ions at dawn than at dusk.

[12] The red arrows in Figures 2 and 3 indicate how far the plasma sheet population extends earthward from a substantial drop in their fluxes, which is regarded as the plasma sheet inner edge. Note that these inner edges are determined from the statistical flux profiles of many THEMIS passes, not a statistical result of the inner edge locations identified individually from each THEMIS pass, like that obtained by *Jiang et al.* [2011]. Under weak convection conditions, the plasma sheet ions extend closer to the Earth than the electrons. While the inner edge of the ion plasma sheet is at $r \sim 4$–$5\ R_E$ at all MLTs, the electron inner edge changes

substantially with MLT, for example, $r \sim 8\ R_E$ at dawn and $11\ R_E$ at dusk. Plasma sheet electron fluxes also vary significantly with MLT, with fluxes in the afternoon sector being at least an order of magnitude lower than those in the postmidnight sector. However, no such strong MLT differences are seen in the magnitudes of energy fluxes for plasma sheet ions. For both ring current electrons and ions, energy fluxes appear to be rather MLT symmetric. The energy fluxes of ring current ions appear slightly higher than plasma sheet ions, however, the energy fluxes of ring current electrons are about an order of magnitude lower than plasma sheet electrons.

[13] As convection becomes higher, the thermal energy of both plasma sheet ions and electrons become higher, with larger increase occurring at larger r. The overall energy fluxes corresponding to the ion thermal energy also becomes slightly higher, but no clear overall energy flux changes are seen for thermal electrons. The inner edges of both the ion and electron plasma sheet move earthward under higher convection. The maximum inward motion of the electron inner edge can be up to almost $3\ R_E$ at dawn, while the change in the ion inner edge is only about $0.5\ R_E$. The change of the electron inner edges with convection strength is consistent with the results of *Jiang et al.* [2011] using the inner edges identified from each THEMIS pass. Contrary to the changes in the plasma sheet, the thermal energy of both ring current ions and electrons remains almost the same as convection increases, while the overall energy fluxes around the thermal energy increases with larger increase seen in ions than in electrons.

[14] Geotail data have shown that the plasma sheet population beyond $r = 8\ R_E$ is quite isotropic [*Kaufmann et al.*, 2002]. Figure 4 shows that both the ion and electron pressures observed by THEMIS are quite isotropic in the region from the tail to $r \sim 4\ R_E$, except near the magnetopause where the perpendicular pressure becomes slightly higher than the parallel one, perhaps due to compression by the magnetopause. In the inner magnetosphere inside $r \sim 4\ R_E$, the perpendicular pressure becomes larger than the parallel component (up to $\sim 20\%$) so that pressure becomes less isotropic.

[15] The above observations clearly show that there are characteristic differences between the plasma sheet and ring current populations, and between the ion and electron plasma sheet, in their thermal energy, energy fluxes, and dependence on location and convection strength. To investigate what processes are responsible for the observed spatial distributions including the above characteristic differences, we used the RCM simulations described in Paper 1 to evaluate particle distributions resulting from adiabatic transport and energization of particles from realistic sources under self-consistent electric and magnetic fields, and to determine the extent to which the simulated distributions can account for the main observed characteristics discussed above.

3. Simulation Results

3.1. Setup for the RCM Runs

[16] The RCM computes adiabatic electric and magnetic drift transport of ions and electrons and the associated energization under self-consistent electric fields through
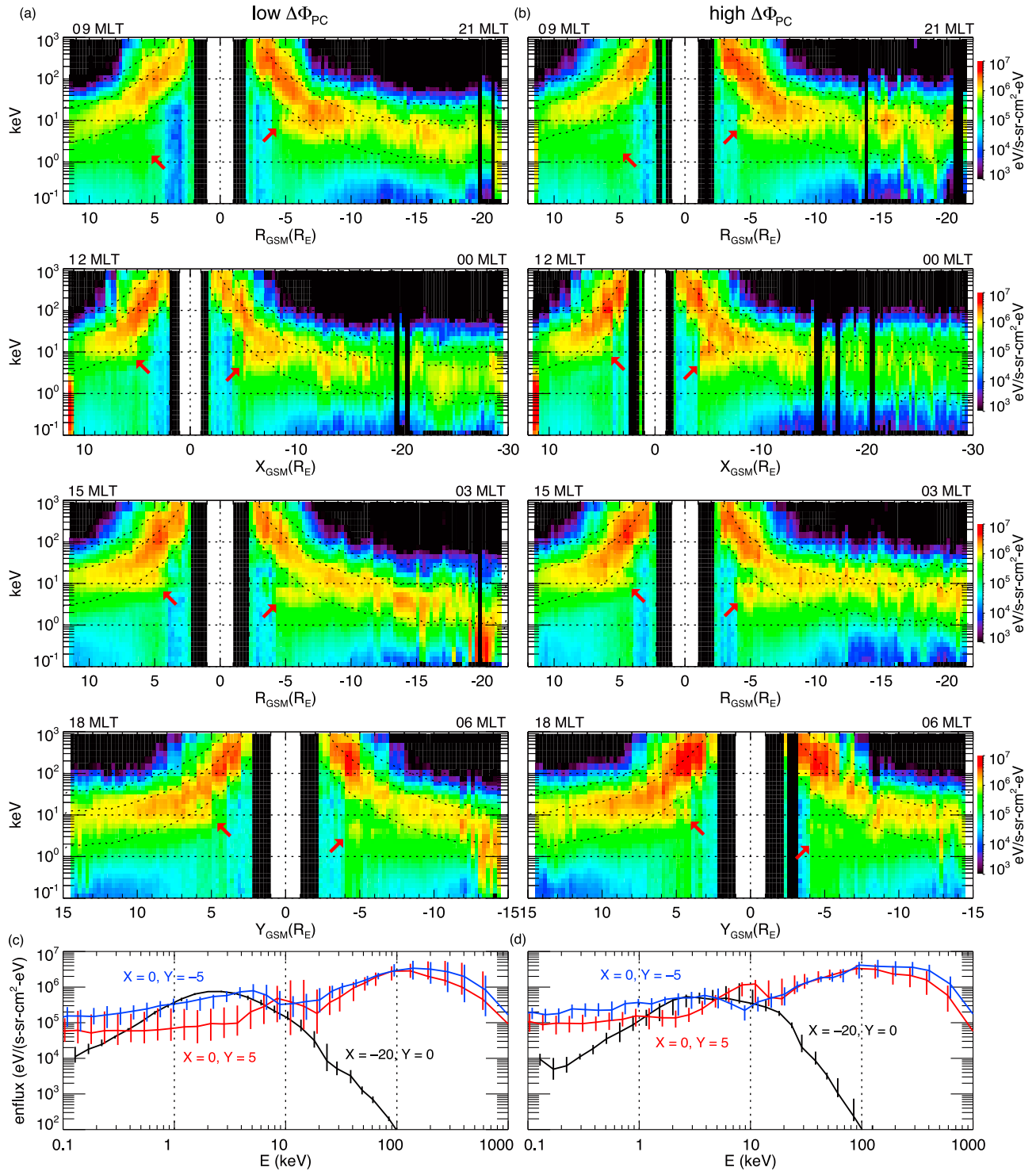
Figure 2. The median values of observed ion energy fluxes (eV/(s sr cm² eV)) along difference MLT meridians indicated in Figure 1 for the (a) low convection level and (b) high convection level. The dotted curves correspond to the energy of three ion λ_k shown in Figure 7. The energy spectrums of median ion energy fluxes (the vertical lines indicated the ranges of 25% and 75% percentiles) under the (c) low convection level and (d) high convection level at $X = -20\ R_E$, $Y = 0\ R_E$ (black), $X = 0\ R_E$, $Y = 4\ R_E$ (red), and $X = 0\ R_E$, $Y = -4\ R_E$ (blue). The red arrows point to the inner edges of the plasma sheet population.
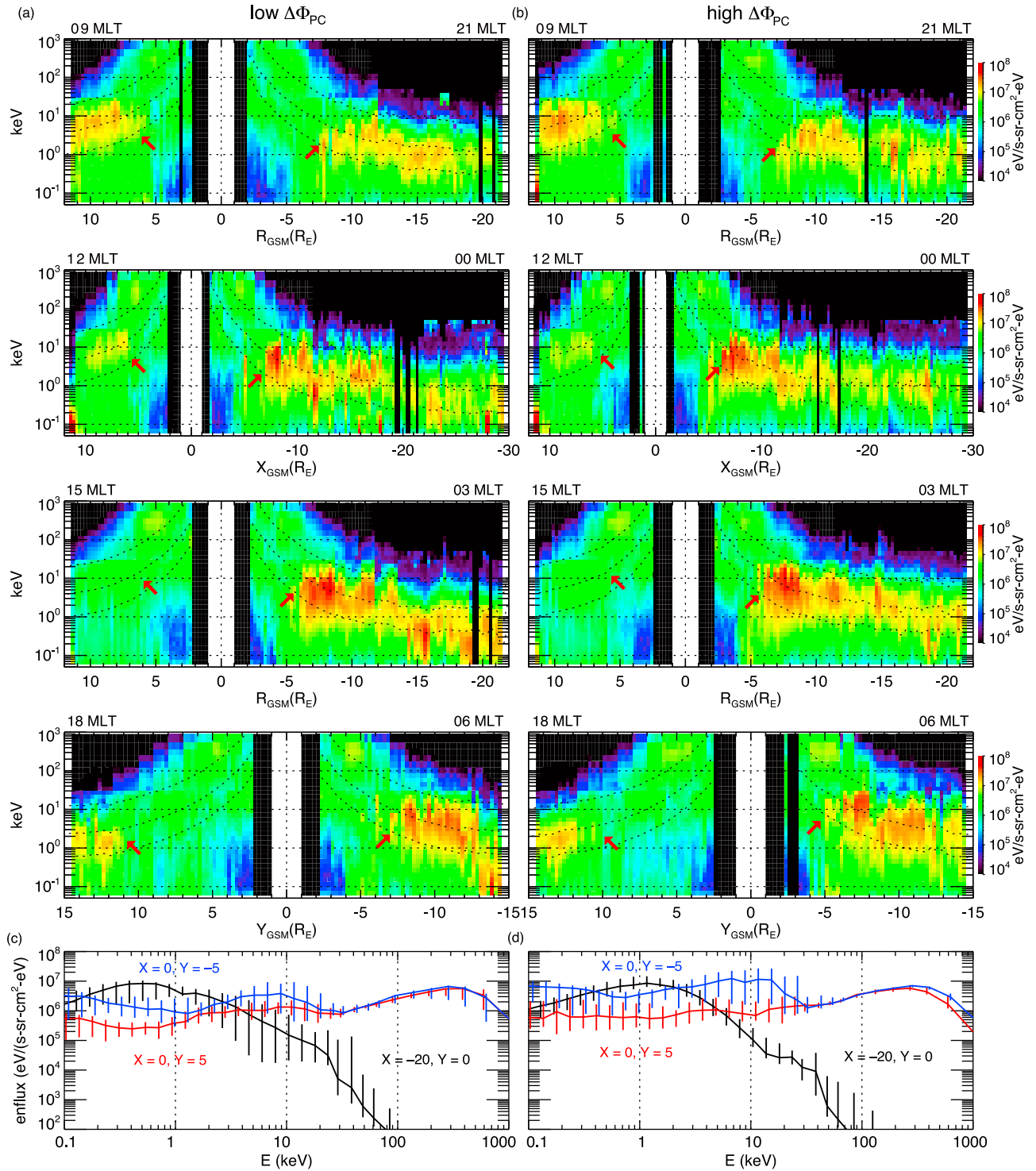
Figure 3. The median values of observed electron energy fluxes (eV/(s sr cm² eV)) along difference MLT meridians indicated in Figure 1 for the (a) low convection level and (b) high convection level. The dotted curves correspond to the energy of three electron λ_k shown in Figure 7. The energy spectrums of median electron energy fluxes (the vertical lines indicated the ranges of 25% and 75%) under the (c) low convection level and (d) high convection level at $X = -20 \ R_E$, $Y = 0 \ R_E$ (black), $X = 0 \ R_E$, $Y = 4 \ R_E$ (red), and $X = 0 \ R_E$, $Y = -4 \ R_E$ (blue). The red arrows point to the inner edges of the plasma sheet population.
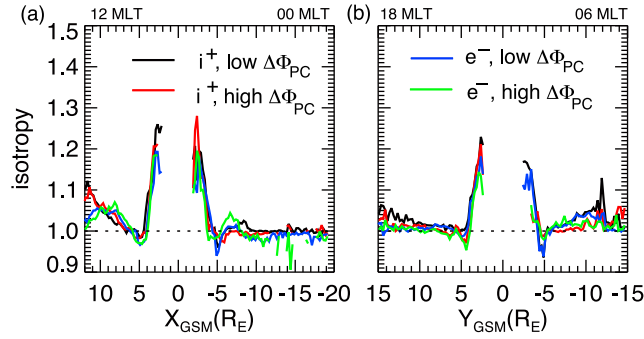
Figure 4. Plasma pressure isotropy ($P_\perp/P_\parallel$) along (a) the noon-midnight meridian and (b) the dawn-dusk meridian for ions under low (black) and high (red) $\Delta\Phi_{PC}$ and for electrons under low (blue) and high (green) $\Delta\Phi_{PC}$.

electrodynamic coupling between the magnetosphere and ionosphere [*Toffoletto et al.*, 2003]. As described in Paper 1, in our RCM runs we incorporated the RCM with a magnetic field solver to provide self-consistent magnetic fields in force balance with the RCM plasma pressures in the equatorial plane.

[17] The inner RCM boundary is set to be at $r = 2\ R_E$ and the outer boundary is defined by a $15\ R_E$ circle with its center at $X = -5\ R_E$ and $Y = 0$. Particle sources are specified at the outer boundary. Source particles may enter into the model depending on the particle's drift velocity at the boundary. To establish particle sources at the RCM outer boundary locations that are consistent with the observations shown in section 3, we selected the observations within a $1\ R_E$ radial distance range centered at the RCM outer boundary for both convection levels. We then fitted the particle distributions with two-component kappa distributions,

$$f = N_c \left(\frac{m}{2\pi\kappa_c E_{0,c}}\right)^{\frac{3}{2}} \frac{\Gamma(\kappa_c + 1)}{\Gamma(\kappa_c - 1/2)} \left[1 + \frac{E}{\kappa_c E_{0,c}}\right]^{-\kappa_c - 1}$$
$$+ N_h \left(\frac{m}{2\pi\kappa_h E_{0,h}}\right)^{\frac{3}{2}} \frac{\Gamma(\kappa_h + 1)}{\Gamma(\kappa_h - 1/2)} \left[1 + \frac{E}{\kappa_h E_{0,h}}\right]^{-\kappa_h - 1}, \quad (1)$$

where f is phase space density, N is density, m is particle mass, and κ and E_0 are parameters of the kappa distribution (subscript c is for cold population and h is for hot populations, E_0 is the energy of the peak particle flux). N, κ, and E_0 are free parameters in the fitting. The fitted parameters are shown in Figure 5. The major differences in the boundary sources between the two convection levels are mainly at the nightside MLT with a more enhanced cold population under weak convection and higher temperature for the hot component under enhanced convection.

[18] In the RCM runs for this study, we model both ions and electrons but include proton as the only ion species. We started the RCM runs with no particles inside the model region so that all the particles appearing at later time must originally come from the outer boundary sources. The objective of the simulation is to investigate if adiabatic transport can deliver these source particles to the MLT and radial distance locations and adiabatically energize them to the energies statistically observed for the plasma sheet and ring current populations under weak and enhanced

convection. Realistic temporal variations of $\Delta\Phi_{PC}$ are often complicated containing various convection strengths and fluctuations. Specification of such complicated variations for a simulation allows for more appropriate comparisons with observations, but it is difficult to distinguish and determine the effects on the resulting distributions from different factors. As a first step to understand the statistical results within the two $\Delta\Phi_{PC}$ ranges, we focus mainly on the effect of the $\Delta\Phi_{PC}$ strength, not its temporal variations, on the simulated distributions. Thus we simplified our convection conditions for the simulation by including two 5 h periods of steady low convection at the beginning and end of the run, and a 3 h period of steady enhanced convection in between. The two changes between the steady low- and high-convection periods were imparted by linearly changing $\Delta\Phi_{PC}$ over the course of 1 h. The time-dependent $\Delta\Phi_{PC}$ and boundary conditions are shown in Figure 5c. We chose 3–5 h for the steady convection intervals simply to allow enough time for the particles from the tail sources to drift to the dayside after $\Delta\Phi_{PC}$ and sources being changed. We then investigate if any of the key features in the statistical distributions can be accounted for by transport under these simple driving conditions.
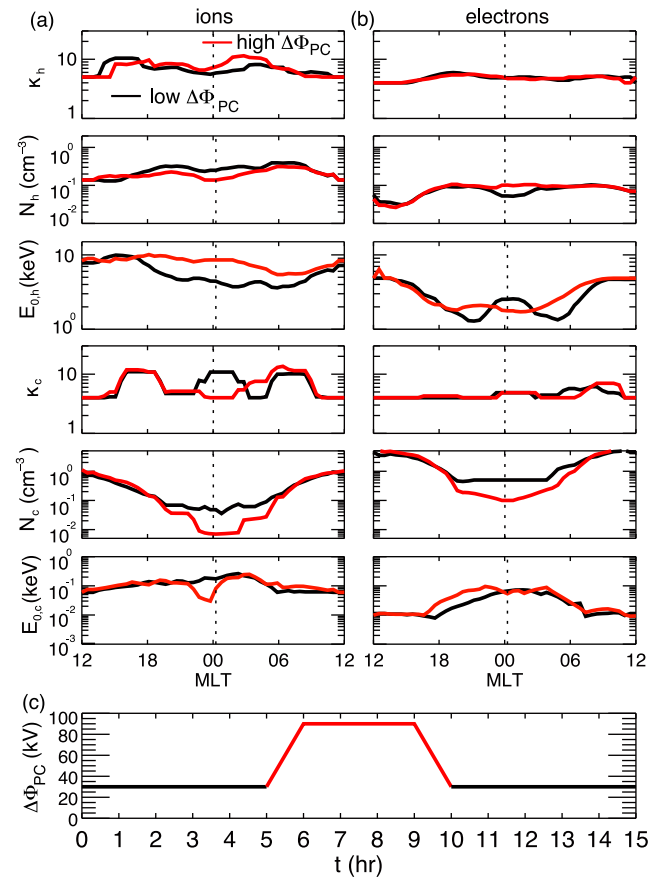

Figure 5. The parameters for the two-component kappa distributions specified at different MLT along the RCM outer boundary for (a) ions and (b) electrons under low (black) and high (red) $\Delta\Phi_{PC}$. (c) Temporal variations of $\Delta\Phi_{PC}$ specified for the RCM run with black (red) indicating the low $\Delta\Phi_{PC}$ (high $\Delta\Phi_{PC}$) boundary condition is applied at the time.
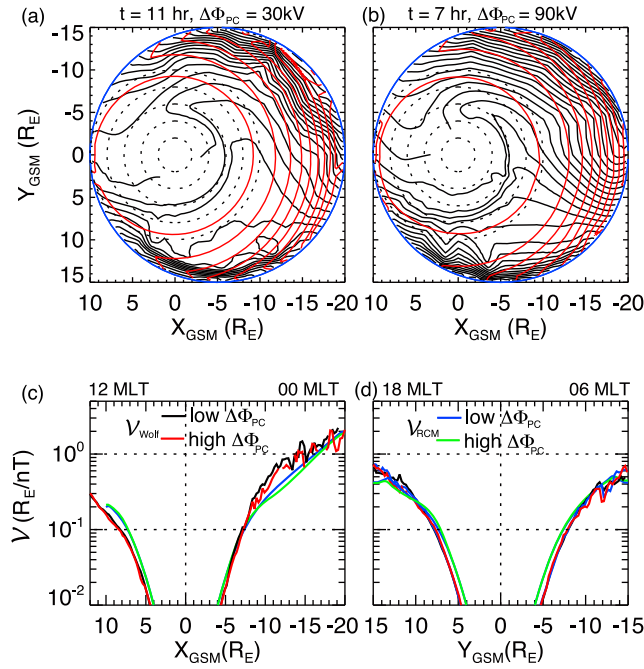
Figure 6. Electric field potential (kV) (the black contours, corotation excluded) and the RCM V (R_E/nT) (the red contours) in the equatorial plane at (a) $t = 11$ h and (b) $t = 7$ h. Contour intervals are 1 kV and 0.2 R_E/nT in Figure 6a and 2.5 kV and 0.2 R_E/nT in Figure 6b. The blue circles in Figures 6a and 6b indicate the RCM outer boundary. The flux tube volumes estimated using the *Wolf et al.* [2006] formula (V_{Wolf}) for the low (black) and high (red) $\Delta\Phi_{PC}$ conditions and the volume from the RCM (V_{RCM}) for the low (blue) and high (green) $\Delta\Phi_{PC}$ conditions along the (c) noon-midnight and (d) dawn-dusk meridians.

3.2. Energy-Dependent Drift Paths and Particle Source Locations

[19] In the RCM, particles of the same energy invariant λ_k ($\lambda_k = E_k \cdot V^{2/3}$, where k is an index for energy channel, E_k is particle kinetic energy, and V is flux tube volume per unit magnetic flux) move along the electric and magnetic drift paths so the total energy $q\Phi + \lambda_k \cdot V^{-2/3}$ is conserved, where q is electric charge (+1 for protons and −1 for electrons) and Φ is electric potential. Therefore the contours of total energy are equivalent to drift paths and drift velocity for λ_k is $\mathbf{V}_k = \mathbf{V}_{k,E} + \mathbf{V}_{k,B} = \mathbf{B} \times \nabla\Phi + \lambda_k\mathbf{B} \times \nabla V^{-2/3}/qB^2$ where $\mathbf{V}_{k,E}$ is electric drift, $\mathbf{V}_{k,B}$ is magnetic drift, and B is magnetic field [*Wolf*, 1983]. Figures 6a and 6b show the contours of convection Φ (the black contours, corotation Φ not included) and V (the red contours) from the RCM run at $t = 11$ h ($\Delta\Phi_{PC} = 30$ kV) and at $t = 7$ h (90 kV), respectively. Figures 6c and 6d show comparisons between the simulated V and the V estimated from the observations using the *Wolf et al.* [2006] formula as described in section 2 under the two convection levels. The simulated V shown in Figure 6 for the low (high) convection level is an average of all Vs corresponding to $30 < \Delta\Phi_{PC} < 40$ kV ($50 < \Delta\Phi_{PC} < 90$ kV) in order to best match the two $\Delta\Phi_{PC}$ ranges of the observation results. In general, the RCM volumes agree with the estimated volumes in both their magnitudes and radial variations. The RCM volumes

are slightly lower than the estimates in the nightside plasma sheet between $r \sim 8$–15 R_E, but both the simulation and observed estimates show a clear change of the dV/dr rates at ~ 8 R_E and a small reduction in volumes on the nightside beyond $r \sim 8$ R_E under stronger convection. Despite that we did not expect an exact match in the volumes, the difference can be partially due to that, as described in Paper 1, the force balance in the off-equatorial region, limited by magnetic field lines being constrained to a "Dungey field line" shape, is not achieved perfectly. Examining the balance at $r \sim 8$–15 R_E shows relatively lower lobe magnetic pressure than the equatorial plasma pressure, implying the field lines being less stretched, thus smaller volumes, than they would be if perfect force balance is achieved.

[20] Currently no magnetopause is imposed on the RCM magnetic fields, thus the RCM volumes near the dayside model boundary, which is close to typical dayside magnetopause locations, are slightly larger than the estimates.

[21] Figure 6 shows that typical electric drift is mainly toward the dayside and diverted around the Earth in the inner magnetosphere due to shielding of convection. Magnetic drift, on the other had, is mainly in the azimuthal direction with ions going westward and electrons eastward. Figure 7 shows contours of total drift paths (corotation drift included) at $t = 11$ h ($\Delta\Phi_{PC} = 30$ kV) and at $t = 7$ h (90 kV) for three different λ_k ($\lambda_k = 0.75, 5,$ and 15 keV-$V_0^{2/3}$ for ions and $\lambda_k = 0.25, 1,$ and 5 keV-$V_0^{2/3}$ for electrons, where $V_0 = 2$ (R_E/nT) is the volume typical at 20 R_E midnight. So the λ_k value thus defined indicates the kinetic energy that a λ_k particle will have at 20 R_E midnight). We chose to show the drift paths at $t = 11$ and 7 h because at these times $\Delta\Phi_{PC}$ have been constant for 1 h after a decrease (an increase) to 30 kV (90 kV) so that the shielding of convection electric field has been well developed and the drift paths have become relatively steady. As can be seen from the energy fluxes corresponding to the three λ_k at midnight 20 R_E shown in Figures 2c and 3c, these λ_k values were specifically chosen to represent the low-energy, thermal-energy, and high-energy particles of the main plasma sheet ion and electron populations, respectively. The change of kinetic energy with r corresponding to these λ_k is shown as dotted curves in Figures 2 and 3 for ions and electrons, respectively. The drift paths that connect to the RCM outer boundary are called open paths, and those that do not are called closed paths. The boundary between open and closed paths as indicated by the blue curves is called the drift path separatrix or Alfvén layer.

[22] Comparing the drift paths in Figure 7 with the contours of Φ and V in Figure 6 clearly shows that transport of the low-energy ions is dominated by electric drift and high-energy ions by magnetic drift, while the thermal-energy ions are determined by both electric and magnetic drift since magnitudes of the two drift speeds are comparable. Because the thermal energy of electrons is low, only the drift paths for high-energy plasma sheet electrons are significantly different from electric drift paths. Owing to increasing azimuthal magnetic drift with increasing particle energy, particles of higher λ_k from the outer boundary have less access to smaller r than do those of lower λ_k from the same boundary location. As a result, there is energy dispersion in the separatrix locations with the separatrix being at larger r with increasing particle energy. Owing to the effect of
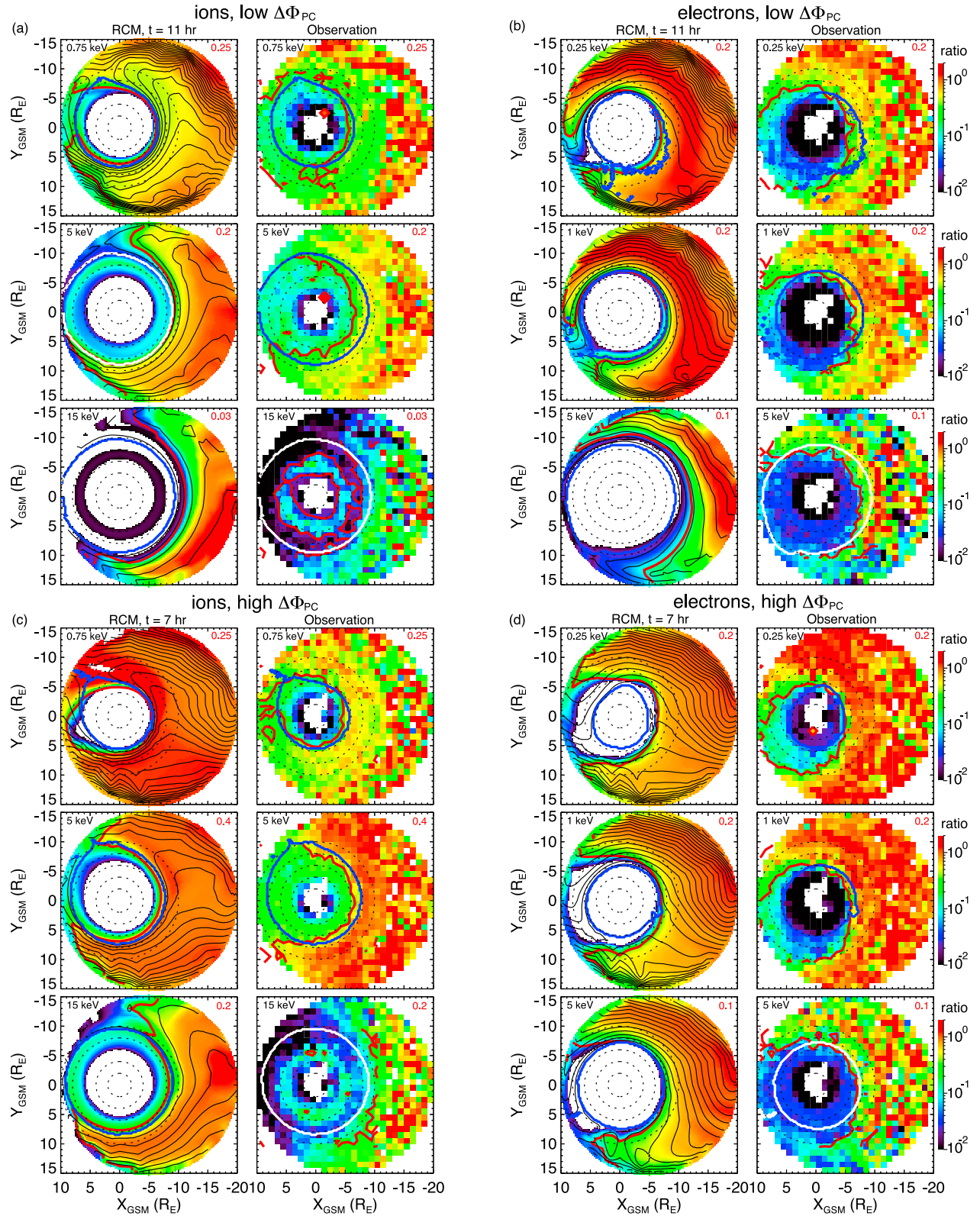
Figure 7. Equatorial distributions of normalized η_k (color contours) for the three representative λ_k (indicated by the energy at the top left corner of each plot) for (a) ions and (b) electrons under low $\Delta\Phi_{PC}$ at $t = 11$ h and for (c) ions and (d) electrons under high $\Delta\Phi_{PC}$ at $t = 11$ h. The RCM results are shown on the left and the observations on the right. The thin black curves superimposed on each RCM plot are the total drift paths (corotation included). The thick blue or white (depending on the background color) enclosed curve indicates the separatrix, and the thick red curve indicates a contour of fixed ratio (the ratio is indicated by the number at the top right corner of each plot; the same ratio is for the RCM and observation).

shielding, electric drift typically diverts eastward in the postmidnight sector, which is roughly in the opposite direction of ion's westward magnetic drift, and diverts westward in the premidnight sector, which is more parallel to ion's magnetic drift. Therefore, for thermal ions that have magnetic drift comparable to electric drift, their total drift directions in the postmidnight sector are significantly different from those in the premidnight sector, resulting in a strong dawn-dusk asymmetry in those particles' open drift paths, and a separatrix that is closer to Earth at dusk than dawn.

[23] For electrons, magnetic drift becomes comparable to electric drift at high λ_k. Since electron's magnetic drift is eastward, the open paths and separatrix location for electrons of high λ_k have a dawn-dusk asymmetry that is opposite to the asymmetry seen at the thermal-energy ions. For electrons of low to thermal energy, their open paths go around the Earth through either dawn or dusk and meet again in the afternoon sector due to the effect from corotation. In addition, $\nabla(q\Phi + \lambda_k V^{-2/3})$ becomes smaller toward the afternoon MLT and magnetic fields become larger as these electrons drift toward the afternoon sector. Thus their speed ($|\mathbf{V}_k| \propto \nabla(q\Phi + \lambda_k V^{-2/3})/B$) becomes very slow, so that takes them relatively long time to reach the afternoon sector. As is discussed later, this long drift time allows for more loss, thus playing a role in causing the low electron particle number content in the afternoon sector.

[24] The open drift paths determine both where particles can go and where they come from, including where their source locations are. For low-energy particles in the plasma sheet, most of them can be traced back to the tail boundary. For ions (electrons) of higher energy, those from the tail sources drift toward dusk (dawn), thus having little access to regions of smaller r, while particles at smaller r are within the open paths that connect to sources at MLT further toward dawn (dusk).

[25] As $\Delta\Phi_{PC}$ changes, so do the spatial distributions of the open paths, as well as their corresponding source locations. Under higher $\Delta\Phi_{PC}$, the separatrices move closer to the Earth and the earthward displacement is larger at lower λ_k since the corresponding drift is more dominated by electric drift. The radial movement of the separatrices indicates that particles in the region next to these separatrices do not constantly remain along an open or closed drift path.

3.3. Spatial Distributions of Ion and Electron Particle Number Content η

[26] Spatial distributions of the number of particles are determined by the spatial distributions of drift paths described above, and how many particles are moving within each of these paths. In the RCM, the number of particles of λ_k within the energy range from $\lambda_{k,min}$ to $\lambda_{k,max}$ and V is defined as particle number content η_k ($\eta_k = 4\pi \cdot 2^{1/2}/m^{3/2} \cdot \int |\lambda_k|^{1/2} \cdot f_k(\lambda)d\lambda$, where m is the particle's mass and f is phase space density, so that $\eta_k = n_k \cdot V$, where n_k is partial number density within the energy channel. Thus for any given energy channel, η_k is a constant times the phase space density). After particles are released from a particle source, η_k is conserved along these particles' drift paths unless there are local particle losses that remove existing particles or local particle sources that add new particles. A local source would be particles coming from the ionosphere. In current

RCM runs we assumed no local particle sources inside the model region, but our observation-based outer boundary particle sources include all the protons that come from either the solar wind or the ionosphere and enter the tail plasma sheet beyond the outer boundary locations. The RCM considers a weak loss for ions due to charge exchange [*Bishop*, 1996], and a strong loss for electrons due to precipitation with a loss rate simply assumed to be 1/3 of strong pitch angle diffusion [*Schumaker et al.*, 1989] for all electron energies at all locations. Particles that hit the inner or outer boundary are also considered lost. Therefore, spatial distributions of η_k in our runs are determined mainly by drift paths and source strengths, as well as by the additional local losses.

[27] The boundary conditions shown in Figure 5 indicate that the source strengths vary significantly with MLT. To show more clearly the MLT asymmetries in η_k distributions, we plot in Figure 7 color contours of η_k normalized to the average η_k within the region of $X = -15$ to $-20 R_E$ and $|Y| \leq 5 R_E$. Figure 7 shows that the η_k distributions for both the low-energy ions and electrons do not change significantly in the nightside magnetosphere. This is because those low-energy particles mainly come from the nightside tail and their source strengths are relatively constant along the nightside tail boundary. There is a slight MLT asymmetry seen on the dayside due to a slight asymmetry in drift paths that allows particles from the dawn MLT source to drift into the afternoon MLT, while particles in the prenoon MLT still come from the tail.

[28] As λ_k increases, the MLT asymmetry in η_k distribution becomes more significant and the asymmetry extends further into the nightside. This is due to the open paths becoming more dawn-dusk asymmetric so that particles can come from source locations that extend for a wider range in MLT as discussed in 3.2, together with the source strength for the high-energy particles decreasing quickly from the nightside to the dayside boundary. For example, as shown in Figure 7, for the high-energy ions under $\Delta\Phi_{PC} = 30$ kV, particles at $X = -10 R_E$ in the premidnight sector come from ~21 to 3 MLT section of the outer boundary, while particles in the postmidnight sector come from 3 to 11 MLT. Since the source strength drops almost an order of magnitude from 21 to 11 MLT, η_k in the postmidnight sector is significantly lower than in the premidnight sector. It also results in a decrease of η_k with decreasing r that is much more significant than seen at lower energy. If source strengths were constant everywhere and there are no losses, then there would be no MLT asymmetry in η_k distributions within open drift paths even if paths are strongly MLT asymmetric.

[29] The ion charge exchange loss is due to ions encountering geocorona. Since the density of geocorona decreases quickly radially outward, this ion loss is only important for particles in the inner magnetosphere. On the other hand, electrons experience strong precipitation loss everywhere along their drift paths. As described in section 3.2, the drift speed for the low to thermal energy electrons becomes smaller toward the afternoon sector, and this long drift time allows for a larger portion of particles being lost through precipitation before they slowly reach afternoon MLT. Therefore, electron η_k in the afternoon sector is significantly lower than their source strengths.
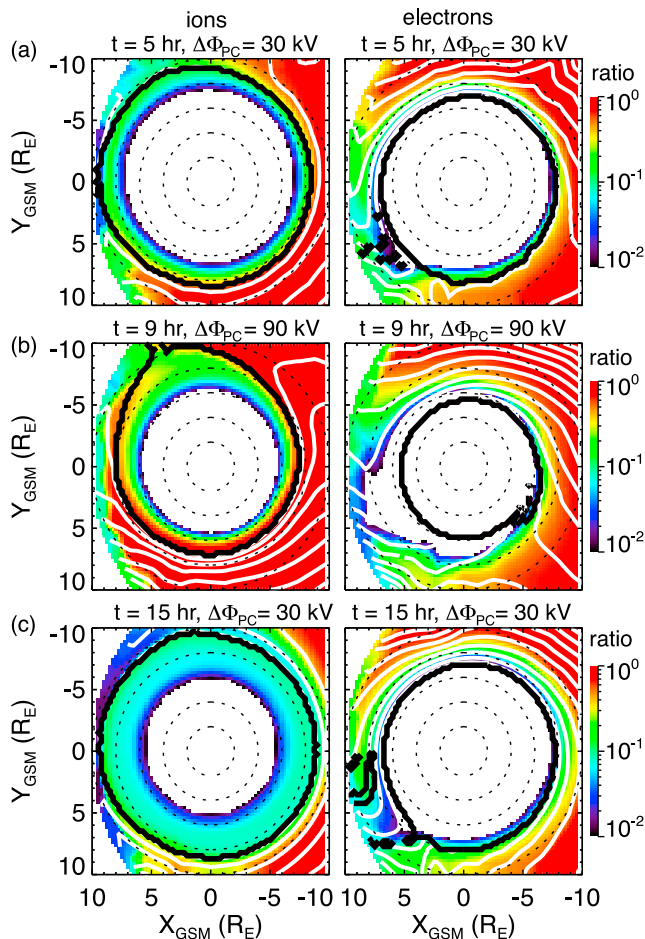
Figure 8. Time sequence of the equatorial distributions of normalized η_k for (left) the thermal ion ($\lambda_k = 5$ keV-$(2\ R_E/$nT$)^{2/3}$) and (right) the thermal electrons ($\lambda_k = 1$ keV-$(2\ R_E/$nT$)^{2/3}$) at (a) $t = 5$ h and $\Delta\Phi_{PC} = 30$ kV, (b) $t = 9$ h and $\Delta\Phi_{PC} = 90$ kV, and (c) $t = 15$ h and $\Delta\Phi_{PC} = 30$ kV. The white contours are total drift paths, and the bold enclosed curves are the separatrices.

[30] If a separatrix is fixed in time and there is no local particle source to add particles into the closed path region, then a step drop of η_k to zero is expected right at the separatrix. As is discussed in the next section, particles can exist within the closed path region because of changes in separatrices, however, the number of those particles within closed paths is relatively small. Therefore, despite not being a sharp step decrease, η_k is seen to decrease radially from the open path to closed path region. The decrease across the separatrix appears sharper at lower energy since their η_k is more uniformly distributed in the open path region, while for the high-energy particles, as discussed above, even in the open path region there is already substantial radial decreases of η_k. To estimate how many particles can be trapped within closed paths, we find a ratio that can best separate particles inside and outside the separatrix for each normalized η_k distribution so that the region where η_k is lower (higher) than that ratio is within the closed (open) paths. These ratios are indicated by the red curve in each RCM η_k distributions in Figure 7 (the ratios are different in each distribution). These ratios are chosen so that the locations of the corresponding red curves

well correlate with the separatrix locations at $t = 7$ and 11 h at most of the nightside MLTs (note that $\Delta\Phi_{PC}$ at both times has been kept constant for 1 h so that the separatrices have become relatively steady). The normalized η_k inside the red curve is smaller than the ratio. Thus the ratios indicate approximately the maximum number of particles that can be trapped within the closed path region predicted by our simulation runs. Since it is impossible to directly determine separatrices from the observations, these same ratios will be applied to the observed η_k distributions to separate particles into regions of open and closed paths.

[31] As $\Delta\Phi_{PC}$ increases, the contribution from electric drift increases, which implies that particles now come from source locations that are confined to a narrower MLT range. This gives relatively more uniform source strengths than during low $\Delta\Phi_{PC}$, and therefore the resulting η_k distributions have less pronounced spatial variations in the open path region. The separatrices move closer to the Earth under higher $\Delta\Phi_{PC}$, and as indicated by the higher maximum ratios for the red curves, more thermal to high-energy ions are able to enter the region that was closed paths during the period of lower $\Delta\Phi_{PC}$.

3.4. Particles Within the Closed Drift Paths

[32] The distributions shown in Figure 7 indicate that there is small but substantial amount of particles within the closed paths. Since initially there are no particles inside the model region and no local sources are specified, these particles must originally come from the outer boundary. Owing to temporal changes in the separatrix locations, particles were previously within open paths can become trapped within closed paths. The changes in the separatrices in our RCM runs can be associated with changes in $\Delta\Phi_{PC}$ that affect drift paths globally and/or development of shielding/overshielding that modifies the paths in the near-Earth magnetosphere. (Note that localized changes in plasma sheet entropy such as those occur during the substorm expansion phase could also affect the locations of the separatrices in a RCM simulation without changing $\Delta\Phi_{PC}$ [e.g., *Zhang et al.*, 2009].) The time sequences in Figure 8 show how the separatrix for thermal energy particles moves with changing $\Delta\Phi_{PC}$. From $t = 0$ to 5 h, despite $\Delta\Phi_{PC}$ remaining constant at 30 kV, gradual development of shielding pushes the separatrix outward, allowing some particles to remain within the closed paths, as can be seen in the small η_k values inside the separatrices at $t = 5$ h. The separatrix moves inward by up to 2 R_E (larger difference for electrons) under $\Delta\Phi_{PC} = 90$ kV at $t = 9$ h. The separatrices then moved outward after $\Delta\Phi_{PC}$ decreased. At $t = 15$ h, the separatrices have returned to almost the same radial distances as at $t = 5$ h, however, there are now many more ions within the closed paths than at $t = 5$ h. This change in drift paths in response to changes in $\Delta\Phi_{PC}$ thus moves significantly more particles from open drift to closed drift paths than does the shielding alone.

[33] For particles that remain within the closed paths, ion particle number content gradually decreases due to the specified weak charge exchange loss, while electrons diminish very quickly due to the strong precipitation loss. As a result, almost no electrons remain within the closed paths at $t = 15$ h. Since the closed drift paths are mostly circular due to corotation being the dominant drift, η_k distributions inside the separatrices are fairly MLT symmetric.

[34] The efficiency of trapping particles within the closed paths depends on the temporal variation of a separatrix relative to the time scale of particle drift, which varies with particle energy. A temporal variation of $\Delta\Phi_{PC}$ including more fluctuations and with a broader period range than that used in our current RCM runs should result in more trapped particles.

4. Comparisons Between the RCM and Observations

[35] In this section we evaluate the extent to which the RCM can account for the observed particle spatial distributions and discuss the likely causes for the differences.

[36] The observed η_k distributions for the three representative λ_k are shown in Figure 7 alongside the RCM results. The observed spatial distributions, despite having very localized variations due to inclusion of data from different periods corresponding to various solar wind and IMF conditions, show clear large-scale variations in r and MLT. Since the separatrices cannot be directly obtained from the observations, we used the η_k ratios obtained from the RCM results in section 3.3 to approximately separate the open and closed drift path regions in the observed η_k distributions particles with the separations indicated by the red curves. The red curves in the observed distributions at nightside MLTs, despite not being at the exact same locations as the RCM separatrices (with the largest difference ~2 R_E), are found to correlate well with the simulated separatrices in their dependences on MLT and on particle energy. The observed normalized η_k in the open path region (outside the red curves) are quite consistent with the RCM results in their magnitudes and MLT asymmetries, in the changes of the asymmetries with particle energy, and in the ion asymmetries being opposite to those of electrons. For electrons of all energies, both observations and simulations show that η_k is the lowest in the afternoon sector.

[37] The observed ion η_k is rather MLT symmetric in the closed path region (inside the red curves), consistent with the RCM results. However, compared with the simulations, the observed ion η_k within the closed path region is larger and extends to much smaller r. The observed ion η_k in the inner magnetosphere can be those that were injected a long time ago in a big storm or perhaps have diffused in over a long period of time, as a result of many increases and decreases in convection. Therefore, the difference can be due to, as we have discussed in section 3.4, the simple $\Delta\Phi_{PC}$ change used for our RCM runs not allowing for realistically efficient trapping of particles. Also for the particles that are already within the closed paths, fluctuations in electric and magnetic fields on a time scale comparable to their drift periods can further diffuse them radially inward. However, Figure 4 shows that the trapped ring current population inside $r < 4$ R_E becomes less isotropic with decreasing r, indicating adiabatic transport and energization of these particles should be more appropriately modeled by conserving their first and second adiabatic invariants than by conserving their energy invariant as used in the RCM. Since the thermal energy of the ionospheric outflow particles is very low, it is not likely that the ionosphere can add particles with such high energy directly into the closed path region. There have been RCM simulations that include processes during the substorm expansion phase

[e.g., *Lemon et al.*, 2004; *Zhang et al.*, 2009; *Yang et al.*, 2011] by changing tail particle sources, and thus particle entropy, quickly and locally. The results show that induced electric fields associated with dipolarization caused by entropy reduction can also inject particles deep into the inner magnetosphere, thus increasing particle number content within the closed path region. This process, however, is not included in our current RCM runs.

[38] Compared with the difference in ion η_k between regions inside and outside the separatrices, the observed electron η_k within the closed path region is much lower than that within the open path region. This indicates the losses for these trapped electrons are stronger than the weak loss for ions, but not as strong as the loss rates specified in our RCM runs, which produces almost no electrons remaining inside the separatrices. Since diffuse electron precipitation occurs outside the plasmapause, which is roughly the separatrices of the low-energy electrons, different loss rates should be specified for electrons inside and outside the separatrices. Additionally, previous studies that compared simulated precipitation electrons with observed diffuse electron aurora [*Chen et al.*, 2005] suggest a more realistic loss rates for electrons within open paths should also depend on location and energy.

[39] Figures 9 and 10 show comparisons of the spectra of η and of energy fluxes along different MLT meridians between the RCM and observations for ions and electrons, respectively. The RCM results in these two figures are averages of the distributions from $t = 5$ to 15 h for two $\Delta\Phi_{PC}$ ranges, $30 < \Delta\Phi_{PC} < 40$ kV for the low convection level and $50 < \Delta\Phi_{PC} < 90$ kV for the high convection level in order to best match the $\Delta\Phi_{PC}$ ranges used in sorting the observations. Since we started the simulations with no particles and it took a few hours for particles from the outer boundary to populate inside the model region, the simulation results before $t = 5$ h are not included in the averages. The RCM reproduces quite well the observed energy dispersions of the separatrices and the magnitudes of η in the region from the separatrices to the model outer boundary. The RCM also accounts for the ions observed in the region earthward of the separatrices. We then convert the RCM η distributions to energy fluxes and compared them with the observations. The comparisons indicate that the observed plasma sheet populations are those within the open paths, and that the observed ring current populations are particles that are within the closed paths and originally come from the plasma sheet. The two populations can exist at the same radial distances since the separatrices of higher-energy particles are located further outward than those of lower-energy particles. The changes of their thermal energy with radial distances are consistent with adiabatic energization. The MLT dependence seen in plasma sheet thermal energy is due to energy-dependent drift. Since ring current population is particles circling around the Earth along closed paths, there is no clear MLT dependence in their thermal energy nor energy fluxes. As $\Delta\Phi_{PC}$ becomes higher, stronger electric drift changes the total drift paths to be more parallel to the direction of V gradients, resulting in larger adiabatic energization. This, together with the changes in particle sources, results in the larger energy fluxes and higher thermal energy for plasma sheet populations observed under higher $\Delta\Phi_{PC}$. The amount of trapped ring current populations depends on the particle addition from the plasma sheet
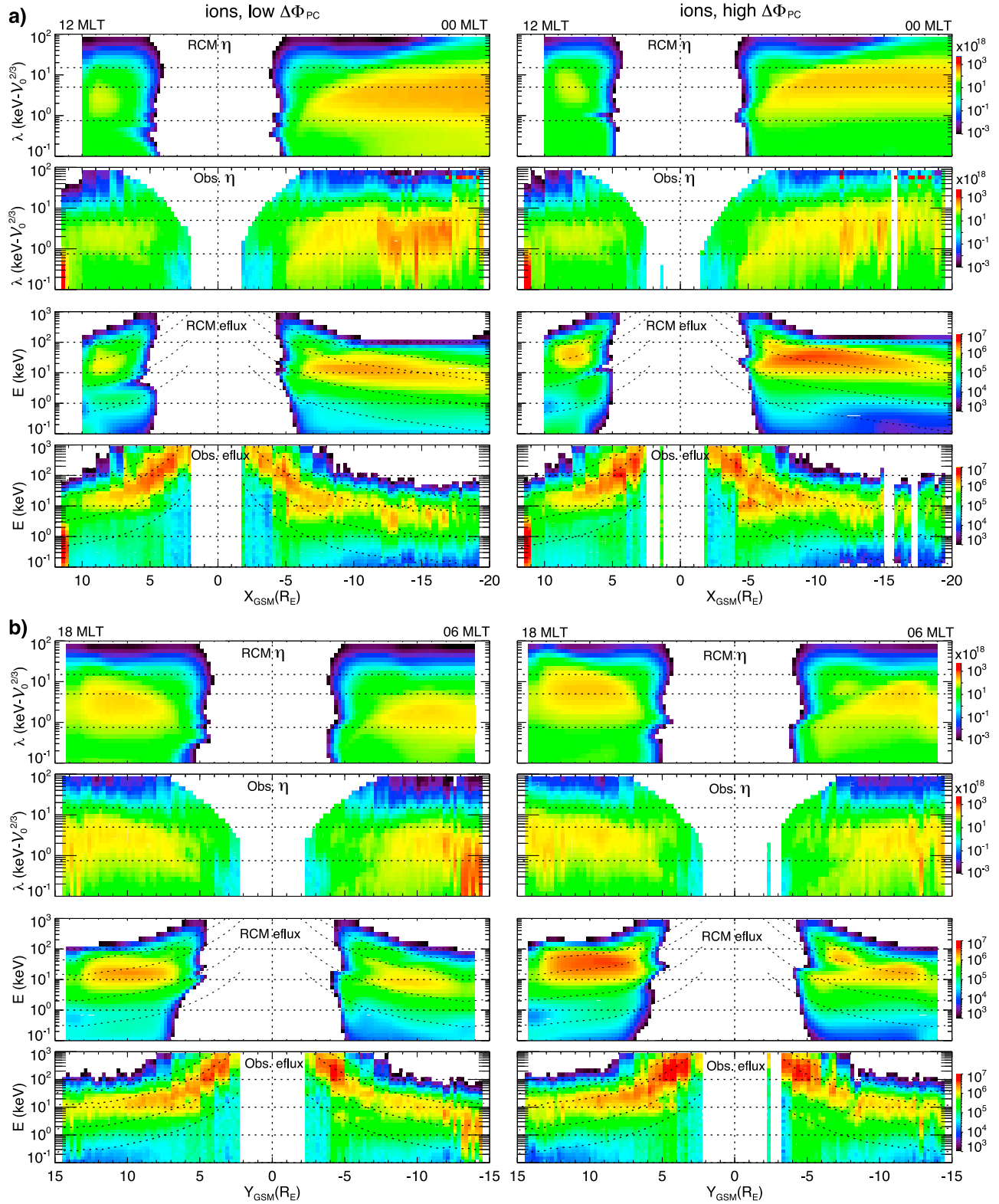
Figure 9. Radial profiles of ion η $(1/(m^2\ T))$ versus λ (keV-$V_0^{2/3}$, where $V_0 = 2\ R_E/nT$) and ion energy flux (eV/(s sr cm^2 eV)) versus energy (keV) from the RCM and observations along (a) the noon-midnight meridian and (b) the dawn-dusk meridian under (left) low $\Delta\Phi_{PC}$ and (right) high $\Delta\Phi_{PC}$.
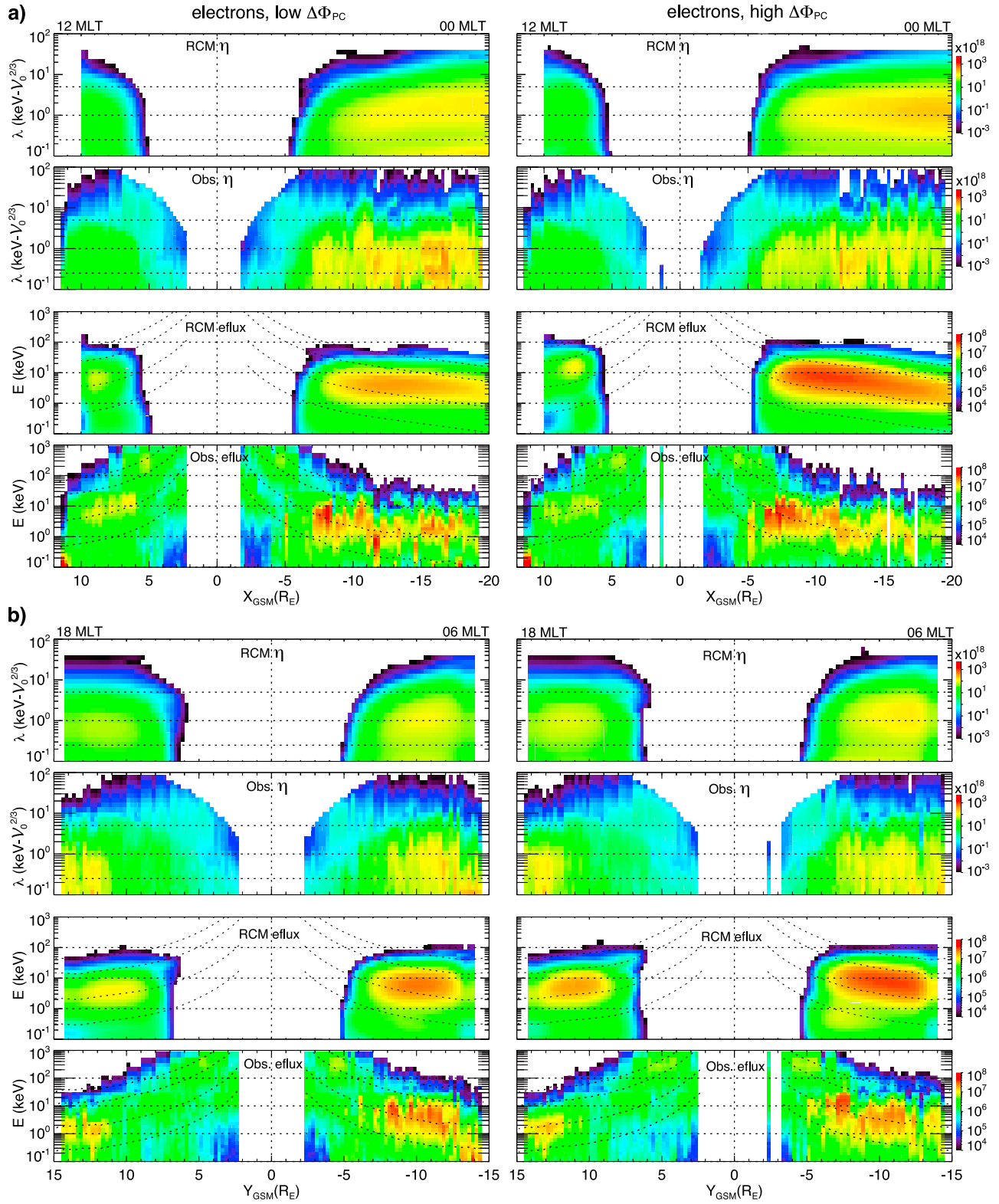
Figure 10. Radial profiles of electron η ($1/(m^2\ T)$) versus λ (keV-$V_0^{2/3}$, where $V_0 = 2\ R_E/nT$) and electron energy flux (eV/(s sr cm^2 eV)) versus energy (keV) from the RCM and observations along the (a) noon-midnight meridian and (b) dawn-dusk meridian under (left) low $\Delta\Phi_{PC}$ and (right) high $\Delta\Phi_{PC}$.

and the losses. Since the specified loss rates do not depend on $\Delta\Phi_{PC}$ and the addition is stronger under higher $\Delta\Phi_{PC}$ when the separatrices move further earthward, ring current energy fluxes become higher under enhanced convection, which can account for the observed changes in ring current ions with convection strength.

[40] As discussed above, the rather simple temporal variations specified for the current RCM runs may not produce sufficient radial diffusion to account for ring current ions being observed to extend to much lower r. For the simulated electrons, those trapped within closed paths were lost too quickly by the specified electron loss to account for the observed ring current electrons. However, the results still suggest that electron loss can explain why the observed energy fluxes of the ring current electrons are much lower than those of plasma sheet electrons. The above differences are not associated with the principles of the RCM physics and are expected to become smaller, based on the above argument, if more realistic specification of the setup for the RCM are used in future studies.

[41] Starting with no particles inside the model domain, plasma sheet and ring current populations are produced in the RCM simulations. Considering that the temporal variations of $\Delta\Phi_{PC}$ and boundary condition used in the current runs are quite simplified compared with the complex variations seen in realistic situations, the RCM can account for several key features of the observed statistical structures of plasma sheet particles, including reproducing the particle number content and the thermal energy that are within the observed ranges, and provide at least qualitative explanation for the characteristics of the observed ring current populations. The results thus clearly indicate that electric and magnetic drift and the associated adiabatic energization, and their changes with $\Delta\Phi_{PC}$ can be the primary processes responsible for the formation and dynamics of the plasma sheet and ring current populations.

5. Summary

[42] The objective of this study is to verify through simulation-observation comparisons if the adiabatic drift transport and associated energization, as used in kinetic models, are the dominant processes responsible for formation and dynamics of plasma sheet and ring current particles. To do the comparisons, we established observed spatial structure of ions and electrons from THEMIS and Geotail measurements and simulated particle distributions using the Rice convection model (RCM).

[43] The observed particle spatial distributions show clear MLT asymmetries in the thermal energy of plasma sheet ions and electrons but rather MLT symmetric thermal energy for ring current particles. The thermal energy of plasma sheet ions in the near-Earth magnetosphere is lower on the dawnside than the duskside, while an opposite asymmetry is observed in plasma sheet electrons. The energy fluxes of plasma sheet electrons show a strong MLT dependence with much lower fluxes in the afternoon sector. Contrary to plasma sheet particles, there are no clear MLT variations in the thermal energy and energy fluxes for ring current ions and electrons.

[44] The RCM runs in this study include both self-consistent electric and magnetic fields, and realistic MLT-dependent particle sources along the model outer boundary established from the observations. Starting with no initial particles, ions and electrons released from the RCM outer sources move inside the model region along adiabatic electric and magnetic drift paths and change their energy adiabatically. The drift paths are either closed or open and the path separatrix is located at larger r with increasing particle energy. The closed drift paths are approximately circular around the Earth due to corotation drift being dominant. For ions, the open drift paths for typical low-energy plasma sheet particles are dominated by sunward electric drift while those for high-energy particles are strongly affected by westward azimuthal magnetic drift. For thermal-energy ions, since their magnetic drift is comparable to electric drift, their open paths are significantly MLT asymmetric, leading these ions to move further toward the duskside than dawnside. For electrons, the MLT asymmetry in their open drift paths is opposite of that of ions because their magnetic drift is eastward. The drift paths and the particle source location to where the open paths connect change with convection strength and the location of separatrices moves inward under stronger convection.

[45] The simulated particle distributions, from comparing with the observed structure, indicate that the particles within open drift paths can account for the observed thermal energy and energy fluxes of plasma sheet populations, and that the significant MLT variations in the spatial distributions are a combined result of species- and energy-dependent drift paths and MLT-dependent particle source strength. The low electron energy fluxes in the afternoon MLT are due to a significant portion of electrons from the tail being lost by strong precipitation before they slowly reached the afternoon sector. The thermal energy and location of the ions trapped within closed paths due to temporal variations of drift paths are found to be consistent qualitatively with the observed ring current ions and their distributions are much more MLT symmetric due to their circular drift paths. Specifying more realistic electron loss rates and temporal variation of convection strength and particle sources for the RCM in future studies should improve agreement with the observed ring current distributions. That the RCM physics can account for the key features seen in the observed distributions of thermal energy and energy fluxes of the plasma sheet and ring current provides solid verification that electric and magnetic drift transport and the associated adiabatic energization play dominant roles in controlling plasma sheet and ring current dynamics.

Appendix A

[46] Energetic electrons in the radiation belts penetrate the THEMIS spacecraft shield and result in energy-independent count rates in ESA [*McFadden et al.*, 2008b]. The automated procedure of removing this contamination evaluates the count rate spectrum and identifies the minimum 3 points in the spectrum and considers their average as the background count rate to be subtracted from all counts. Typically these minima are at low energies, where geophysical fluxes are low. The statistical noise is high for low fluxes, and to overcome that we used a scale factor of 1.5 for the background. This factor was found to result in energy-time spectra that show the least effect from the presence of
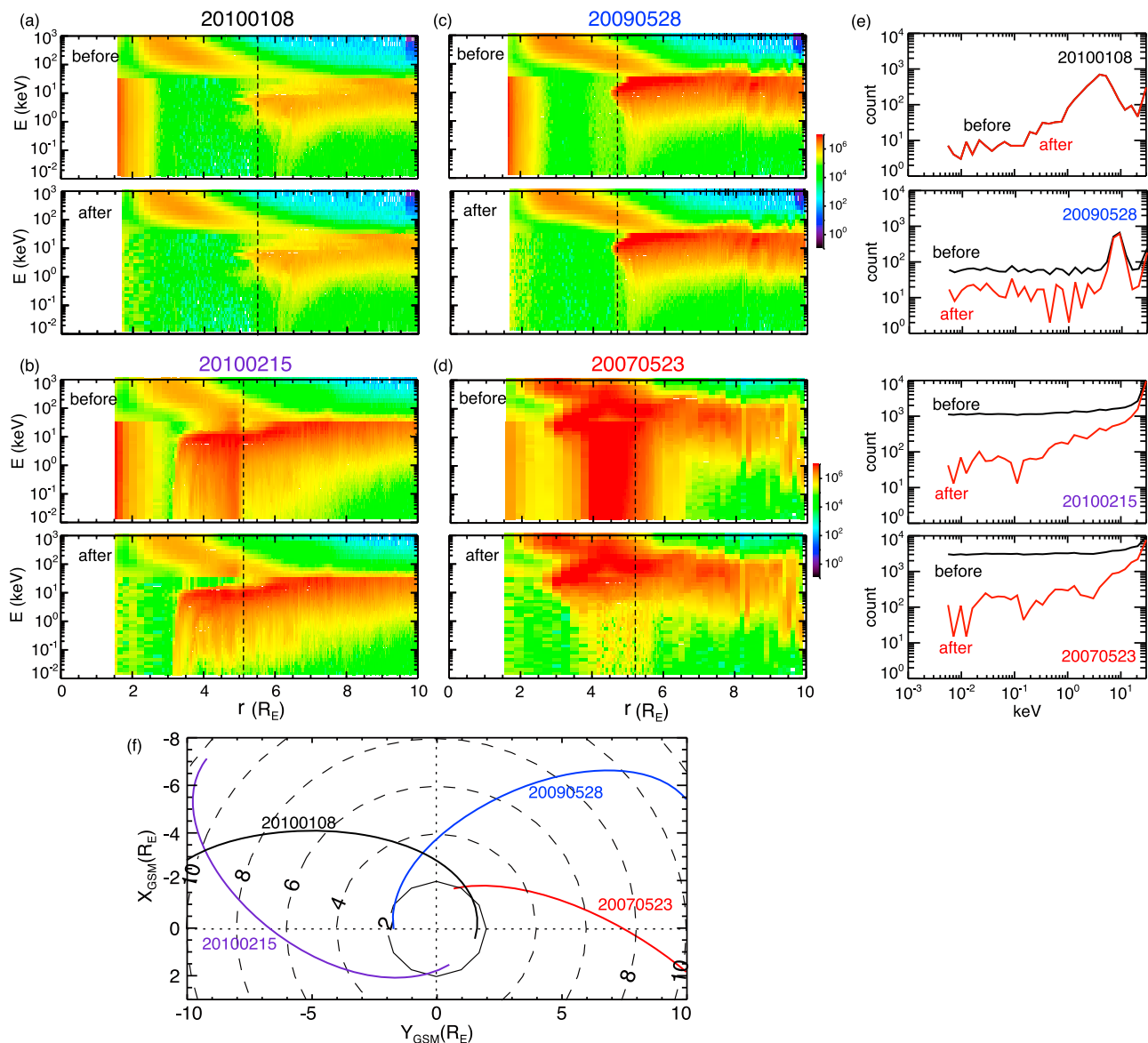
Figure A1. Radial profiles of ion energy fluxes (eV/(s sr cm^2 eV)) versus energy from the THEMIS-D pass on (a) 20100108, (b) 20100215, (c) 20090528, and (d) 20070523 (top) before and (bottom) after removing radiation contamination. (e) Comparison of the count number before and after removing contamination at a radial distance indicated by the vertical dashed lines in Figures A1a–A1d. (f) X-Y projection of the THEMIS-D trajectories for the four passes.

penetrating electrons or from the subtraction process itself. The background subtraction is done on each anode independently, as each anode is affected by a different shielding mass, and thus has different response to an ambient energetic spectrum. Note that because the fluxes at low energies are extremely low and especially at higher altitude, the typical value for background subtraction in the absence of penetrating electrons (at low or high altitudes) is zero, and thus application of this subtraction process has a small effect beyond 8 R_E. Oversubtraction is, however, avoided by limiting the background subtraction to times when the energetic electrons in the 50–100 keV range as measured by the SST instrument have flux >5 × 10^5 eV/s sr cm^2 eV.

[47] Figures A1a–A1d show examples of the energy spectrums before and after removing radiation contamination

using the above procedure from four different passes of THEMIS-D. For the 20100108 pass, as shown in Figure A1e, no contamination is removed from the particle distribution at $r = 5.5$ R_E since the SST flux in the 20–100 keV range is below 5 × 10^5 eV/s sr cm^2 eV.

References

Auster, H. U., et al. (2008), THE THEMIS fluxgate magnetometer, *Space Sci. Rev.*, *141*, 235–264, doi:10.1007/s11214-008-9365-9.

Bishop, J. (1996), Multiple charge exchange and ionization collisions within the ring current-geocorona-plasmasphere system: Generation of a secondary ring current on inner L shells, *J. Geophys. Res.*, *101*, 17,325–17,336, doi:10.1029/95JA03468.

Buzulukova, N., M.-C. Fok, A. Pulkkinen, M. Kuznetsova, T. E. Moore, A. Glocer, P. C. Brandt, G. Tóth, and L. Rastätter (2010), Dynamics of ring current and electric fields in the inner magnetosphere during disturbed periods: CRCM-BATS-R-US coupled model, *J. Geophys. Res.*, *115*, A05210, doi:10.1029/2009JA014621.

Chen, M. W., M. Schulz, P. C. Anderson, G. Lu, G. Germany, and M. Wüest (2005), Storm time distributions of diffuse auroral electron energy and X-ray flux: Comparison of drift-loss simulations with observations, *J. Geophys. Res.*, *110*, A03210, doi:10.1029/2004JA010725.

Chen, M. W., S. Liu, M. Schulz, J. L. Roeder, and L. R. Lyons (2006), Magnetically self-consistent ring current simulations during the 19 October 1998 storm, *J. Geophys. Res.*, *111*, A11S15, doi:10.1029/2006JA011620.

Fok, M.-C., N. Buzulukova, S.-H. Chen, P. W. Valek, J. Goldstein, and D. J. McComas (2010), Simulation and TWINS observations of the 22 July 2009 storm, *J. Geophys. Res.*, *115*, A12231, doi:10.1029/2010JA015443.

Gkioulidou, M., C.-P. Wang, L. R. Lyons, and R. A. Wolf (2009), Formation of the Harang reversal and its dependence on plasma sheet conditions: Rice convection model simulations, *J. Geophys. Res.*, *114*, A07204, doi:10.1029/2008JA013955.

Gkioulidou, M., C.-P. Wang, and L. R. Lyons (2011), Effect of self-consistent magnetic field on plasma sheet penetration to the inner magnetosphere: RCM simulations combined with modified Dungey force-balanced magnetic field solver, *J. Geophys. Res.*, doi:10.1029/2011JA016810, in press.

Iglewicz, B., and D. Hoaglin (1993), *How to Detect and Handle Outliers, ASQC Basic Ref. in Qual. Control*, vol. 16, edited by P. D. Mykytka, ASQC Quality, Milwaukee, Wis.

Jiang, F., M. G. Kivelson, R. J. Walker, K. K. Khurana, V. Angelopoulos, and T. Hsu (2011), A statistical study of the inner edge of the electron plasma sheet and the net convection potential as a function of geomagnetic activity, *J. Geophys. Res.*, *116*, A06215, doi:10.1029/2010JA016179.

Jordanova, V. K., S. Zaharia, and D. T. Welling (2010), Comparative study of ring current development using empirical, dipolar, and self-consistent magnetic field simulations, *J. Geophys. Res.*, *115*, A00J11, doi:10.1029/2010JA015671.

Kaufmann, R. L., C. Lu, W. R. Paterson, and L. A. Frank (2002), Three-dimensional analyses of electric currents and pressure anisotropies in the plasma sheet, *J. Geophys. Res.*, *107*(A7), 1103, doi:10.1029/2001JA000288.

Kokubun, S., T. Yamamoto, M. H. Acuna, K. Hayashi, K. Shiokawa, and H. Kawano (1994), The Geotail magnetic field experiment, *J. Geomagn. Geoelectr.*, *46*, 7–21, doi:10.5636/jgg.46.7.

Korth, A., R. H. W. Friedel, C. G. Mouikis, J. F. Fennell, J. R. Wygant, and H. Korth (2000), Comprehensive particle and field observations of magnetic storms at different local times from the CRRES spacecraft, *J. Geophys. Res.*, *105*, 18,729–18,740, doi:10.1029/1999JA000430.

Kurita, S., et al. (2011), Transport and loss of the inner plasma sheet electrons: THEMIS observations, *J. Geophys. Res.*, *116*, A03201, doi:10.1029/2010JA015975.

Lemon, C., R. A. Wolf, T. W. Hill, S. Sazykin, R. W. Spiro, F. R. Toffoletto, J. Birn, and M. Hesse (2004), Magnetic storm ring current injection modeled with the Rice convection model and a self-consistent magnetic field, *Geophys. Res. Lett.*, *31*, L21801, doi:10.1029/2004GL020914.

McFadden, J. P., C. W. Carlson, D. Larson, V. Angelopoulos, M. Ludlam, R. Abiad, B. Elliott, P. Turin, and M. Marckwordt (2008a), The THEMIS ESA plasma instrument and in-flight calibration, *Space Sci. Rev.*, *141*, 277–302, doi:10.1007/s11214-008-9440-2.

McFadden, J. P., C. W. Carlson, D. Larson, J. Bonnell, F. Mozer, V. Angelopoulos, K.-H. Glassmeier, and U. Auster (2008b), THEMIS ESA first science results and performance issues, *Space Sci. Rev.*, *141*, 477–508, doi:10.1007/s11214-008-9433-1.

Milillo, A., S. Orsini, and I. A. Daglis (2001), Empirical model of proton fluxes in the equatorial inner magnetosphere: Development, *J. Geophys. Res.*, *106*, 25,713–25,729, doi:10.1029/2000JA900158.

Mukai, T., S. Machida, Y. Saito, M. Hirahara, T. Terasawa, N. Kaya, T. Obara, M. Ejiri, and A. Nishida (1994), The low-energy particle (LEP) experiment onboard the Geotail satellite, *J. Geomagn. Geoelectr.*, *46*, 669–692, doi:10.5636/jgg.46.669.

Roeder, J. L., M. W. Chen, J. F. Fennell, and R. Friedel (2005), Empirical models of the low-energy plasma in the inner magnetosphere, *Space Weather*, *3*, S12B06, doi:10.1029/2005SW000161.

Schumaker, T. L., M. S. Gussenhoven, D. A. Hardy, and R. L. Carovillano (1989), The relationship between diffuse auroral and plasma sheet electron distributions near local midnight, *J. Geophys. Res.*, *94*, 10,061–10,078, doi:10.1029/JA094iA08p10061.

Toffoletto, F., S. Sazykin, R. Spiro, and R. Wolf (2003), Inner magnetospheric modeling with the Rice convection model, *Space Sci. Rev.*, *107*, 175–196.

Wang, C.-P., L. R. Lyons, J. M. Weygand, T. Nagai, and R. W. McEntire (2006), Equatorial distributions of the plasma sheet ions, their electric and magnetic drifts, and magnetic fields under different interplanetary magnetic field B_z conditions, *J. Geophys. Res.*, *111*, A04215, doi:10.1029/2005JA011545.

Wang, C.-P., L. R. Lyons, T. Nagai, J. M. Weygand, and R. W. McEntire (2007), Sources, transport, and distributions of plasma sheet ions and electrons and dependences on interplanetary parameters under northward interplanetary magnetic field, *J. Geophys. Res.*, *112*, A10224, doi:10.1029/2007JA012522.

Wang, C.-P., L. R. Lyons, V. Angelopoulos, D. E. Larson, J. McFadden, S. Frey, U. Auster, and W. Magnes (2008), THEMIS observations of penetration of the plasma sheet into the ring current region during a magnetic storm, *Geophys. Res. Lett.*, *35*, L17S14, doi:10.1029/2008GL033375.

Wang, C.-P., L. R. Lyons, R. A. Wolf, T. Nagai, J. M. Weygand, and A. T. Y. Lui (2009), The plasma sheet PV5/3 and nV and associated plasma and energy transport for different convection strengths and AE levels, *J. Geophys. Res.*, *114*, A00D02, doi:10.1029/2008JA013849.

Weimer, D. R. (1995), Models of high-latitude electric potentials derived with a least error fit of spherical harmonic coefficients, *J. Geophys. Res.*, *100*, 19,595–19,608, doi:10.1029/95JA01755.

Weimer, D. R. (2004), Correction to "Predicting interplanetary magnetic field (IMF) propagation delay times using the minimum variance technique," *J. Geophys. Res.*, *109*, A12104, doi:10.1029/2004JA010691.

Weimer, D. R., D. M. Ober, N. C. Maynard, M. R. Collier, D. J. McComas, N. F. Ness, C. W. Smith, and J. Watermann (2003), Predicting interplanetary magnetic field (IMF) propagation delay times using the minimum variance technique, *J. Geophys. Res.*, *108*(A1), 1026, doi:10.1029/2002JA009405.

Williams, D. J., R. W. McEntire, C. Schlemm II, A. T. Y. Lui, G. Gloeckler, S. P. Christon, and F. Gliem (1994), Geotail energetic particles and ion composition instrument, *J. Geomagn. Geoelectr.*, *46*, 39–57, doi:10.5636/jgg.46.39.

Wolf, R. A. (1983), The quasi-static (slow-flow) region of the magnetosphere, in *Solar Terrestrial Physics*, edited by R. L. Carovillano and J. M. Forbes, pp. 303–368, D. Reidel, Norwell, Mass.

Wolf, R. A., V. Kumar, F. R. Toffoletto, G. M. Erickson, A. M. Savoie, C. X. Chen, and C. L. Lemon (2006), Estimating local plasma sheet PV5/3 from single-spacecraft measurements, *J. Geophys. Res.*, *111*, A12218, doi:10.1029/2006JA012010.

Yang, J., R. A. Wolf, and F. R. Toffoletto (2011), Accelerated thinning of the near-Earth plasma sheet caused by a bubble-blob pair, *Geophys. Res. Lett.*, *38*, L01107, doi:10.1029/2010GL045993.

Zhang, J.-C., R. A. Wolf, R. W. Spiro, G. M. Erickson, S. Sazykin, F. R. Toffoletto, and J. Yang (2009), Rice convection model simulation of the substorm-associated injection of an observed plasma bubble into the inner magnetosphere: 2. Simulation results, *J. Geophys. Res.*, *114*, A08219, doi:10.1029/2009JA014131.

V. Angelopoulos, Department of Earth and Space Sciences, University of California, Los Angeles, CA 90095, USA.

M. Gkioulidou, L. R. Lyons, and C.-P. Wang, Department of Atmospheric and Oceanic Sciences, University of California, Los Angeles, CA 90095, USA. (cat@atmos.ucla.edu)

A. T. Y. Lui, Johns Hopkins University Applied Physics Laboratory, Laurel, MD 20723, USA.

T. Nagai, Department of Earth and Planetary Sciences, Tokyo Institute of Technology, Tokyo 152-8551, Japan.

J. M. Weygand, Institute of Geophysics and Planetary Physics, University of California, Los Angeles, CA 90095, USA.

R. A. Wolf, Department of Physics and Astronomy, Rice University, Houston, TX 77251, USA.